# Global mapping of Titan's surface using an empirical processing method for the atmospheric and photometric correction of Cassini/VIMS images

Stéphane Le Mouélic, Thomas Cornet, Sébastien Rodriguez, Christophe Sotin, Jason Barnes, Kevin Baines, Robert Brown, Axel Lefèvre, Bonnie Buratti, Roger Clark, et al.

## To cite this version:

Stéphane Le Mouélic, Thomas Cornet, Sébastien Rodriguez, Christophe Sotin, Jason Barnes, et al.. Global mapping of Titan's surface using an empirical processing method for the atmospheric and photometric correction of Cassini/VIMS images. Planetary and Space Science, 2012, 73, pp.178 - 190. ⟨10.1016/j.pss.2012.09.008⟩. ⟨hal-03657801⟩

**HAL Id: hal-03657801**

**https://u-paris.hal.science/hal-03657801v1**

Submitted on 12 Oct 2022

Planetary and Space Science ▮ (▮▮▮▮) ▮▮▮–▮▮▮

Contents lists available at SciVerse ScienceDirect

Planetary and Space Science

journal homepage: www.elsevier.com/locate/pss

# Global mapping of Titan′s surface using an empirical processing method for the atmospheric and photometric correction of Cassini/VIMS images

Stéphane Le Mouélic [a,*], Thomas Cornet [a], Sébastien Rodriguez [b], Christophe Sotin [a,c], Jason W. Barnes [d], Kevin H. Baines [c], Robert H. Brown [e], Axel Lefèvre [a], Bonnie J. Buratti [c], Roger N. Clark [f], Philip D. Nicholson [g]

[a] Laboratoire de Planétologie et Géodynamique de Nantes, CNRS UMR 6112, Université de Nantes, 2 rue de la Houssinière, BP 92208, 44322 Nantes, Cedex 3, France
[b] Laboratoire AIM, Université Paris 7/CNRS/CEA, Centre de l′Orme des Merisiers, Bât. 709, 91191 Gif/Yvette Cedex, France
[c] Jet Propulsion Laboratory, California Institute of Technology, 4800 Oak Grove Drive, Pasadena CA 91109, USA
[d] Department of Physics, University of Idaho, Engineering-Physics Building, Moscow ID 83844, USA
[e] Departments of Planetary Sciences and Astronomy, University of Arizona, Tucson, USA
[f] United States Geological Survey, Denver CO 80225, USA
[g] Department of Astronomy, Cornell University, Ithaca, NY 14853, USA

## ARTICLE INFO

*Article history:*
Received 5 March 2012
Received in revised form
14 September 2012
Accepted 17 September 2012

*Keywords:*
Titan
Surface
Infrared
Cassini
VIMS
Hyperspectral

## ABSTRACT

We have processed all images of Titan's surface acquired by the Visual and Infrared Mapping Spectrometer between 2004 and 2010, with the objective of producing seamless global mosaics of the surface in the six infrared atmospheric windows at 1.08, 1.27, 1.59, 2.03, 2.6–2.7 and 5 μm. A systematic study of the photometry at 5 μm, where haze scattering can be neglected, shows that the surface behaves to first order like a Lambert surface. The results at 5 μm are generalized to lower wavelengths, adding an empirical correction accounting for scattering from atmospheric aerosols, using methane band wings as a proxy for the calculation of the scattering additive term. Mosaics incorporating this empirical correction for the geometry and haze scattering show significantly less seams than any previous maps integrating data acquired over such a wide range of observing geometries, and may therefore be used for the study of surface properties. We provide several suggestions for further studies aimed at improving the global mapping of the surface of Titan. With the considered thresholds limits on the acquisition parameters, we found that 13% of Titan's surface has been mapped at an instrument resolution better than 10 km/pixel, 56% of the surface was seen at a resolution between 10 and 20 km/pixel, and 24% of the coverage falls in the range 20–50 km/pixel.

## 1. Introduction

The Visual and Infrared Mapping Spectrometer (VIMS) onboard Cassini acquires hyperspectral images of Titan in 352 spectral channels from 0.3 to 5.1 μm (Brown, 2004). Infrared channels are particularly useful to map the surface of Titan through narrow atmospheric transmission windows, which allows geomorphological studies thanks to the imaging capabilities (Sotin, 2005; Rodriguez et al., 2006; Barnes et al., 2007a, 2007b, 2008; Le Mouélic et al., 2008; Jaumann et al., 2009). The spectral dimension can be used to investigate the composition of surface materials (Mc Cord et al., 2008, Clark et al., 2010, Moriconi et al., 2010). A significant issue to be solved is the deconvolution between atmospheric and surface signals. This problem is relevant both for the retrieval of surface reflectivity and also for the mapping of spectral units. Merging data acquired during different flybys with very different viewing geometries (incidence, emergence and phase angles), is a very challenging task due to the strong contributions of the atmosphere (additive and multiplicative components) and also due to surface photometric properties. This causes uncorrected mosaics to appear with seams, which hampers the precise determination of surface spectral heterogeneities (Stefan et al., 2009).

The surface and atmospheric physical properties of Titan have been investigated using high-fidelity radiative transfer codes in the UV–visible–NIR range using doubling-adding algorithms or discrete-ordinates approximations. These models, which include absorption by the atmospheric gases and multiple scattering by hazes, have been used to analyze images or spectra of Titan recorded during telescopic observation campaigns (Griffith et al., 1991, 2003), or more recently by VIMS observations (Rannou et al., 2010). However, complete radiative transfer codes are usually very time consuming, which precludes their use on a global scale. They may also still face residual uncertainties linked for example to a lack of knowledge of physical parameters such as gas absorption coefficients under the

---

* Corresponding author. Tel.: +33 0 2 51 12 54 65; fax: +33 2 51 12 52 68.
*E-mail address:* stephane.lemouelic@univ-nantes.fr (S. Le Mouélic).

0032-0633/$ - see front matter © 2012 Elsevier Ltd. All rights reserved.
http://dx.doi.org/10.1016/j.pss.2012.09.008

Please cite this article as: Le Mouélic, S., et al., Global mapping of Titan′s surface using an empirical processing method for the atmospheric and photometric.... Planetary and Space Science (2012), http://dx.doi.org/10.1016/j.pss.2012.09.008

relevant environmental conditions, aerosols optical properties and/or distribution of these species. Our goal here is not to fully solve the complex problem of the deconvolution of surface and atmospheric effects. Rather it is to provide some empirical considerations that do not fully treat the radiative transfer problem, but that are complementary to it because they can be easily applied to global mosaics. In this paper, we therefore focus on data processing methods and on an empirical approach for reducing the atmospheric component in VIMS images, with the objective of building homogeneous global mosaics of the surface in the six atmospheric windows at 1.08, 1.27, 1.59, 2.03, 2.6–2.7 and 5 μm.

The calibrated VIMS data set is described in Section 2, where we present spatial and spectral filtering strategies aiming at improving the sharpness of surface images. In Section 3 we present the computation of a global mosaic integrating all the data acquired between Ta (October 2004) and T70 (June 2010), with a first focus on the correction of the mosaic in the 5 μm window, which is the least affected by the additive atmospheric aerosol scattering (Rodriguez et al., 2006). We then study the more complex case of shorter wavelength images, using an empirical approach to mitigate the effects of the additive aerosol scattering. We finally conclude with the perspectives for further studies aimed at producing fully homogenized mosaics in all atmospheric windows.

## 2. Description of the global VIMS data set

### 2.1. Data content and radiometric calibration

The VIMS instrument acquires up to 64 × 64 pixels images in 352 narrow spectral channels from 0.3 to 5.1 μm (Brown, 2004). The instrument is constituted of two channels: (1) VIMS-V uses a 2D CCD, with 96 spectral channels covering the range from 0.35 to 1.04 μm, (2) VIMS-IR uses a linear detector, with 256 spectral channels covering the range from 0.88 to 5.10 μm. In this paper we focus on the VIMS-IR only, as the surface of Titan can hardly be seen using a VIMS-V telescope (Vixie et al., 2012). For VIMS-IR, the spectral sampling is 16.6 nm, and the pixel's instantaneous field of view is 0.5 × 0.5 mrad$^2$. The two dimensions of the image are obtained using two perpendicular scanning mirrors. A high resolution mode can be used in one dimension, providing pixels with a field of view 0.25 × 0.5 mrad$^2$. Raw data are calibrated and converted into units of $I/F$, where $I$ is the specific intensity and $\pi F$ is the incoming solar flux, using the procedures described by Brown (2004) and Barnes et al. (2007a).

An example of calibrated cube and spectra of bright and dark regions is given in Fig. 1. The surface of Titan can be directly observed by VIMS-IR through the atmosphere in narrow infrared windows at 1.08, 1.27, 1.59, 2.03, 2.7-2.8 and 5 μm, that we will later refer to as "atmospheric windows", where the atmospheric gases absorption is the weakest. The scattering by the atmospheric aerosols at short wavelength induces a blurring effect that will be discussed later. Wavelengths outside the atmospheric windows probe mostly the upper layers of the atmosphere, as shown for example on the 1.22 μm image in Fig. 1.

### 2.2. Spatial enhancement of the images

The best images in terms of contrast are acquired in the 2 μm window, which presents the best compromise between sufficiently high signal-to-noise ratio (S/N) (decreasing with increasing wavelength, along with the decreasing incident solar flux) and sufficiently low atmospheric scattering (an effect decreasing with increasing wavelength). As already mentioned in Le Mouélic et al. (2008), we noted that the image contrast and sharpness can be improved by using a series of processing steps, which include: 1- coadding spectral channels where surface is discernable within methane windows, 2-oversampling the original cube by a factor of two to four, 3- applying a bilinear interpolation filter in order to smooth the pixels in the oversampled image, 4- applying an unsharp mask procedure. In a case of a 64 × 64 images, a good trade-off for the unsharp mask is to use a kernel size of 6 pixels and a gain close to 0.5. Two examples of this processing pipeline are given in Fig. 2 on high resolution 64 × 64 images acquired respectively during the Ta and T4 flybys on Tortola Facula and on dunes in Fensal. Dune fields significantly show up more clearly in the T4 image after the spatial enhancement. This step might therefore be very useful for geomorphological studies, in addition to precise geocoding. The unsharp masking should not be used if the spectral information is needed, as this algorithm modifies the overall $I/F$ level.

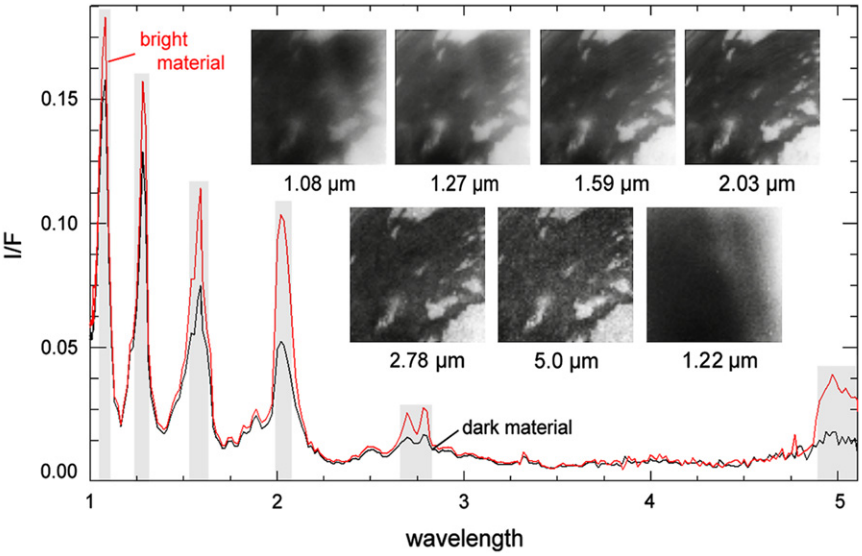

**Fig. 1.** Example of a VIMS high resolution cube of Titan acquired during the T4 flyby (cube CM_1490991359_4, 31th March, 2005 with a spatial sampling ranging from 1.7 to 2.5 km/pixel). The surface can be seen in six narrow atmospheric windows centered at 1.08, 1.27, 1.59, 2.03, 2.7–2.8 and 5 μm. Other wavelengths probe mostly the atmosphere, as shown for example by the image taken at 1.22 μm.

Please cite this article as: Le Mouélic, S., et al., Global mapping of Titan′s surface using an empirical processing method for the atmospheric and photometric.... Planetary and Space Science (2012), http://dx.doi.org/10.1016/j.pss.2012.09.008

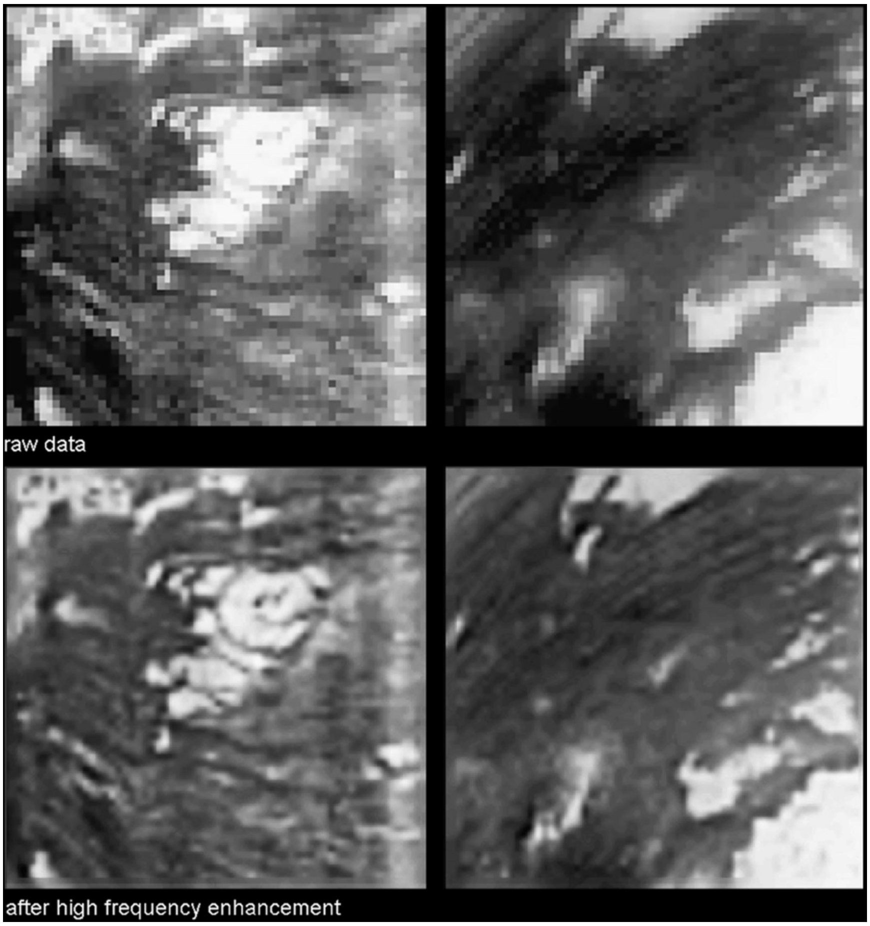

**Fig. 2.** Example of spatial enhancement applied to VIMS images. The left column corresponds to the cube labeled CM_1477496141, acquired the 26th October 2004 (Ta) with a spatial sampling ranging from 1.8 to 2.6 km/pixel. The right column corresponds to the cube CM_1490991359_4 acquired the 31th March, 2005 (T4), with a spatial sampling ranging from 1.7 to 2.5 km/pixel. Top: raw images at 2.03 μm. Bottom: same images after spatial enhancement (co-addition of 12 bands in atmospheric windows, oversampling by a factor of four, bilinear interpolation and unsharp mask procedure). Dunes clearly show up in the processed T4 image.

### 2.3. *Spectral filtering*

As the flybys of Titan occur at a speed of ~20,000 km/h, the design of the VIMS observations is often a trade-off between surface coverage (which is increased by using short exposure times) and signal-to-noise ratio (S/N, which is increased when using long exposures times, but then at the expense of spatial coverage, in particular when we observe near the closest approach). In the complete VIMS data archive, the exposure times range from 13 ms for images taken at closest approach to more than 1000 ms. A saturation effect is often observed in the short wavelength range when using exposure times longer than 300 ms. Long-time exposure observations can still prove to be very useful to obtain a high signal-to-noise in the broad 5 μm atmospheric window, where subtle spectral signatures of hydrocarbons have been identified (Clark et al., 2010; Moriconi et al., 2010).

In the case of very short exposure times, the S/N ratio becomes very low, even at the short wavelengths. Fig. 3 shows two subsets of images acquired in line mode (a.k.a. ‘noodle mode’, which uses the scanning mirror in only one dimension, the second dimension of the image being provided by the spacecraft motion) at 13 ms during the T20 flybys on a bright-dark boundary named Chosuk Planitia (Jaumann et al., 2008), and on a dune field in fensal (Barnes et al., 2008). Fig. 3a shows RGB composites using $R=1.59/1.27$ μm, $G=2.03/1.27$ μm, $B=1.27/1.08$ μm ratios built from the original image produced by the standard calibration pipeline. Fig. 3b shows the same ratios after a refinement of the dark frame correction, which is particularly useful in line mode acquisition in order to remove strong “stripped” artifacts.

A significant improvement of the S/N ratio of VIMS images acquired with a short exposure time can be obtained by using the Minimum Noise Fraction (MNF) transform (Boardman and Kruse, 1994). The number of spectral channels acquired by VIMS-IR (256) is much higher than the number of sources of intrinsic variability of a given scene. The MNF algorithm is used to determine the inherent dimensionality of image data, and then to segregate and equalize the noise in the data. The MNF transform uses two cascaded Principal Components direct transformations. The first one decorrelates and rescales the noise in the data. The second transform is a standard Principal Components direct transformation of the noise-whitened data. The resulting bands of the MNF transformed data are ranked with the largest amount of variance in the first few bands and decreasing data variance with increasing band number until only noise and no coherent image remains.

When applied to the 256 VIMS infrared channels, we see that only the very first MNF bands contain signal with significant spatial coherence. This is illustrated in Fig. 3c, which presents the first 5 bands of the MNF transform of the data shown in Fig. 3b. The smooth appearance of the first band in the upper panel is primarily due to atmospheric variations, which dominate the signal. Surface features can often be found within the next few MNF bands (MNF bands 2, 3 and 4 in the upper panel, and MNF bands 1, 2 and 3 in the lower panel). Surface signal can also be found in up to 10–15 MNF components depending on the signal contained in the

Please cite this article as: Le Mouélic, S., et al., Global mapping of Titan′s surface using an empirical processing method for the atmospheric and photometric.... Planetary and Space Science (2012), http://dx.doi.org/10.1016/j.pss.2012.09.008

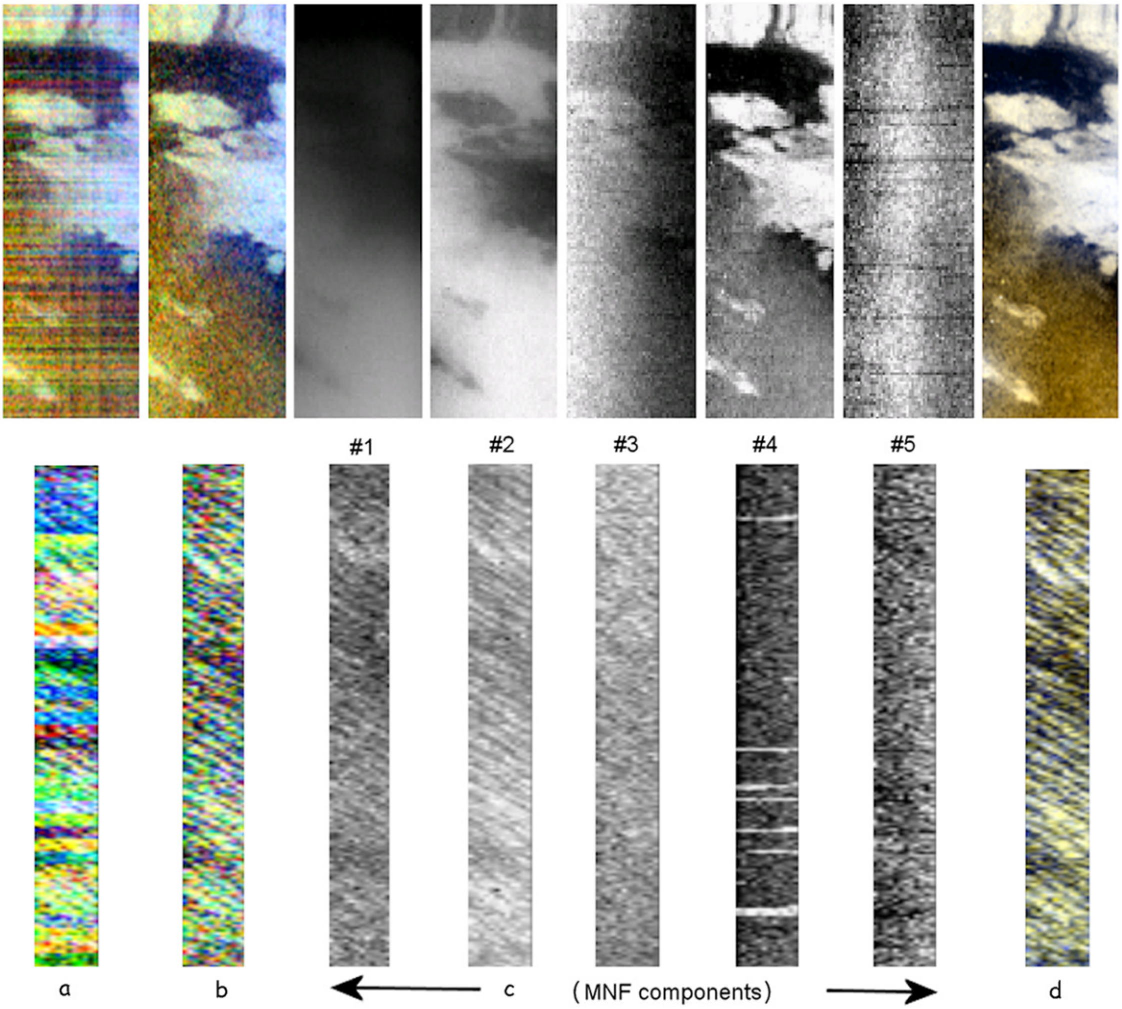

**Fig. 3.** Illustration of the MNF spectral filtering for short exposure time images (13 ms) acquired on October 25th, 2006 on Chosuk Planitia (top) and Fensal dune fields (bottom). (a) RGB composites using $R=1.59/1.27$ µm, $G=2.03/1.27$ µm, $B=1.27/1.08$ µm. (b) Same images after the a refined dark frame correction. (c) First 5 components of the direct MNF transform. (d) Same images as (b) after filtering by the inverse MNF transform of direct MNF bands 2, 3 and 4 (top) and 1,2 and 3 (bottom).

input data cube. Bands 5 and higher in the upper panel of Fig. 3c contain only noise, as do bands 4, 5 and higher in the lower panel of Fig. 3c. An inverse MNF transform is applied with the MNF bands showing coherent patterns only, which significantly reduces the inherent noise of the hyperspectral cube. This is illustrated in Fig. 3d. Sharper color images of the surface can therefore be obtained by using a successive combination of the MNF filtering and the spatial enhancement shown in Fig. 2. The MNF filtering can also be used to increase the signal-to-noise ratio of the spectra themselves. However, even if this method is useful to locally improve the mapping as clearly shown by Fig. 3d, we do not recommend its use for spectral studies, as it could slightly alter the shape of the most subtle spectral features.

### 2.4. Merging the complete data set from October 2004 to June 2010 into a global mosaic

After discussing data reduction and processing tips for single image cubes, we now focus on the integration of the cubes into a global mosaic. In order to integrate all the available VIMS imagery acquired during the nominal and equinox missions (from Ta to T70) into a single global hyperspectral mosaic, we have automatically sorted the complete list of VIMS cubes (representing more than 20,000 image cubes of Titan) in order of spatial resolution. In the final mosaic, coarse resolution images are used as background with progressively finer resolution images overlain on top. We have applied an oversampling by a factor of two and a bilinear interpolation to the cubes in order to smooth out the pixels before filling their corresponding location in the final mosaic. A series of filters has been designed to remove pixels acquired with extreme observing geometries, because they produce strong atmospheric artifacts. In particular, we used thresholds of 80° for the incidence ($i$) and emergence ($e$) angles. A lower threshold would produce a map with less intense seams (due to atmospheric effects and surface photometry), but we would then miss interesting areas such as Hotei Regio or the northern lakes, which have never been observed under favorable illuminating conditions. In the same manner, we also used a threshold of 100° for the phase angle, and a threshold of 7 for the total airmass. The total airmass, defined as $1/\cos(i)+1/\cos(e)$, corresponds to the total optical path length of the light (incoming and outgoing) through the atmosphere, relative to that at the zenith. The mosaic presented in this work contains only cubes acquired with exposure times in the range 40–260 ms to avoid exceedingly noisy images and saturated pixels. Finally, the global mosaic has been produced at a resolution of 32 pixels per degree, corresponding to a spatial sampling of 1.4 km per pixel at the equator.

Fig. 4 (left) shows the global mosaic in a cylindrical projection centered at 0° west in three atmospheric windows at 1.08, 2.03 and 5 µm and in a wavelength at 1.95 µm probing only the atmosphere. The corresponding acquisition geometry is shown in Fig.4 (right).

Please cite this article as: Le Mouélic, S., et al., Global mapping of Titan′s surface using an empirical processing method for the atmospheric and photometric.... Planetary and Space Science (2012), http://dx.doi.org/10.1016/j.pss.2012.09.008

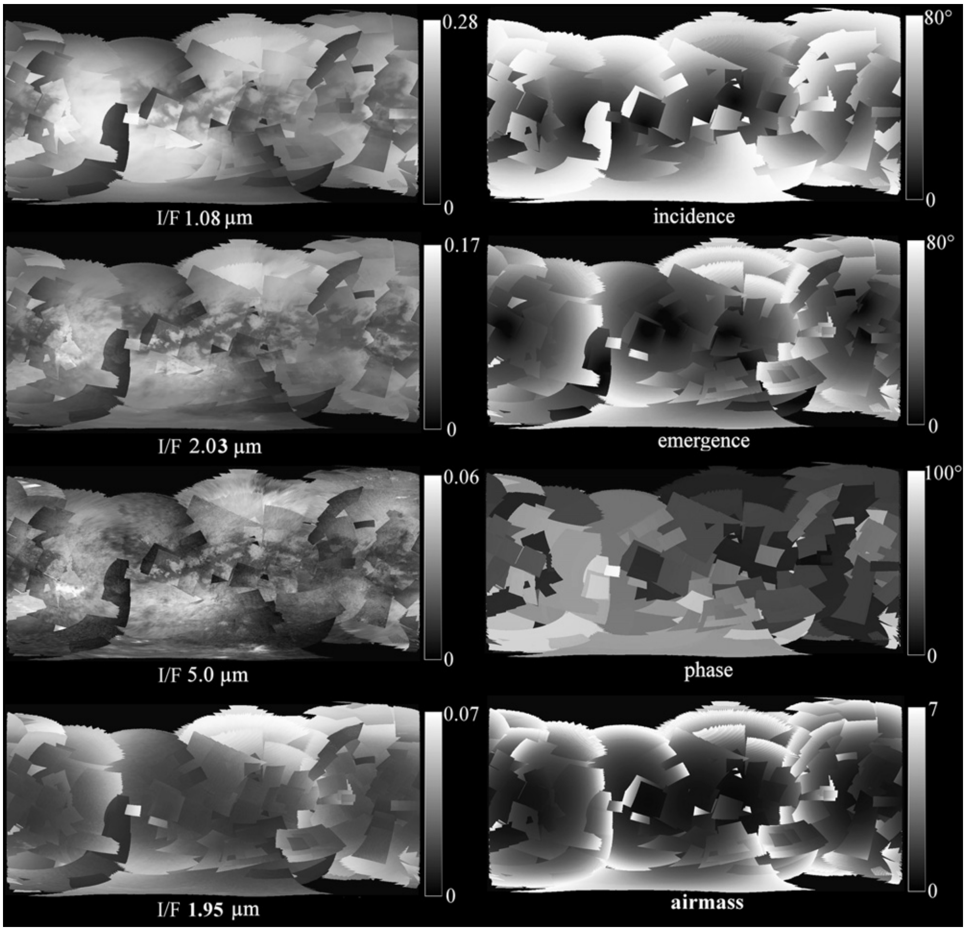

**Fig. 4.** Left: global mosaics of Titan in a cylindrical projection centered on 0° west in three atmospheric windows (1.08, 2.03 and 5 μm) and in a wavelength probing only the atmosphere (1.95 μm). All the individual cubes that compose the mosaic were acquired during the Cassini nominal and Equinox missions between Ta (October 2004) and T70 (June 2010), with exposure times ranging from 40 and 260 ms, with $i < 80°$, $e < 80°$, phase $< 100°$ and airmass $< 7$. Right: observing geometry for all images used in the mosaic. Images acquired over wide ranges of incidence, emission, and phase angles and airmasses are incorporated into the mosaic. Significant seams due to atmospheric effects and uncorrected surface photometry appear between individual images. Values are indicated with a linear gray scale.

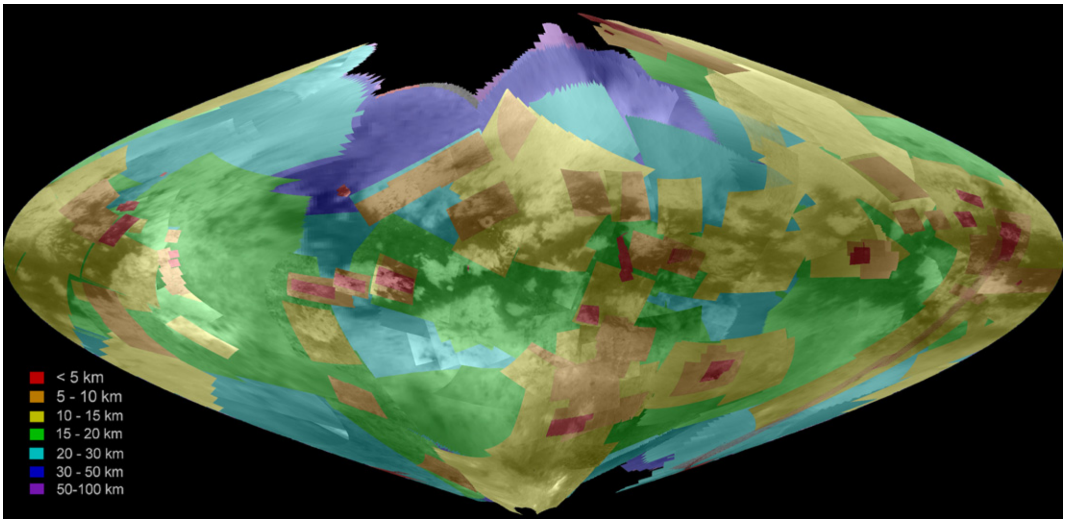

**Fig. 5.** Spatial resolution of the VIMS cubes acquired between Ta and T70. The 2 μm image is used as a transparent background with a sinusoidal projection. Only 13% of the surface has been seen with a resolution better than 10 km/pixel during the nominal and equinox missions.

The 5 μm mosaic is the average of 14 spectral channels taken between 4.88 and 5.11 μm. We see that significant seams appear at all wavelengths, and that the contrast of surface features decreases with decreasing wavelength. This is due both to atmospheric effects, which are more important for short wavelengths, and to the uncorrected illumination variations. The apparent blurring is mostly due to the aerosol scattering. With the considered threshold limits on the acquisition parameters, we found that only ~2% of the surface has been seen at a resolution better than 5 km/pixels between Ta and T70. 11% of the surface was seen with a resolu-

Please cite this article as: Le Mouélic, S., et al., Global mapping of Titan′s surface using an empirical processing method for the atmospheric and photometric.... Planetary and Space Science (2012), http://dx.doi.org/10.1016/j.pss.2012.09.008

tion in the 5–10 km/pixel range, 31% at 10–15 km/pixel, 25% at 15–20 km/pixel, 18% at 20–30 km/pixel, 6% at 30–50 km/pixel, and 4% of the surface remains uncovered (Fig. 5).

## 3. Correction of the global mosaic and derivation of the reflectance of bright terrains

We define by I($i$,$e$,$\phi$,$\lambda$) the observed spectral radiance at the detector (in W/m$^2$/μm/sr), with $i$, $e$, $\phi$ and $\lambda$ being the incidence, emergence, phase angle and wavelength, respectively. If $J$ is the collimated solar irradiance at the source (in W/m$^2$/μm), in the case of an airless body, then the bidirectional reflectance $r$ ($i$,$e$=$\phi$) of the surface is equal to $I$/J. From Hapke, 1993, equation 10.5, the radiance factor RADF can be written as $RADF(i,e,\phi)=\pi \times \mathrm{r}\ (i,e,\phi)=\pi\ \mathrm{I/J}$.

In the VIMS calibration pipeline, the data are calibrated with respect to a solar spectrum (Thekekara, 1973) corresponding to the solar flux at the instantaneous Sun–target distance, to arrive at $I/F$ (Barnes et al., 2007a). In Hapke et al., 2012, $I/F$ corresponds to the radiance factor, the radiance relative to a perfectly diffusing Lambert surface illuminated normally. This is consistent with the previous formulation, with $J=\pi F$. If we also consider the extinction by the atmosphere, we can finally summarize the problem using the following simplified equation:

$$I(i,e,\phi,\lambda)=F(\lambda)\ RADF(i,e,\phi)\ \exp(-\tau_{atm}(\lambda)\times airmass) + I_{scattered}(i,e,\phi,\lambda) \quad (1)$$

where $\tau_{\mathrm{atm}}$ is the vertical optical depth of the atmosphere, and $I_{\mathrm{scattered}}$ an additive term that includes the light scattered by the atmosphere. In the case of a surface following a Lambert behavior, then $RADF=\cos(i)\times$ constant. The $I/F$ in a surface window free of atmospheric effects should therefore be directly correlated to cos ($i$). In the case of an airless body following the Lommel–Seeliger law, which has been widely used to characterize planetary surfaces, $I/F$ varies with cos $i$/ (cos $i$+cos $e$) at constant phase angle (Hapke 1993, equation 10.5). This dependence will first be tested on the 5 μm window, for which the influence of the atmosphere is minimal.

### 3.1. Analysis of the 5 μm atmospheric window

Rodriguez et al. (2006) showed using both a first order radiative transfer model and an empirical approach that there is almost no additive scattering component at 5 μm. In an area of constant reflectance values, if the optical depth of the atmosphere is negligible, the $I/F$ at 5 μm should be directly correlated to cos($i$) in the case of a Lambertian surface, or to cos $i$/(cos $i$+cos $e$) in the case of a surface following the Lommel–Seeliger scattering law. Fig. 6a and b show the 2D scatter plot of the $I/F$ at 5 μm versus the two geometric factors, computed on all the pixels contained within a latitudinal belt comprised between 20°N and 58°N, corresponding to mostly homogenously bright terrains. This region is low enough in latitude to avoid the effects of the northern polar cloud and its surrounding mist which has been observed north of 60° (Le Mouélic et al., 2012), and contains significant variations of incidence and emergence angles over areas of an apparently similar surface composition. The data in Fig. 6 appear limited to cos($i$) greater than 0.173 due to the 80° threshold on the incidence angle which was used in the building of the mosaic.

We see in Fig. 6a that the $I/F$ at 5 μm is indeed correlated to cos($i$). The 2D scatter plot can be fitted using a straight line with the following equation: $R_5$ μm=0.05$x$ $cos(i)$. Fig. 6b shows that there is less correlation in the case of the Lommel–Seeliger scattering law. This will be further seen in the corrected 5 μm maps (Fig. 7). We have also investigated a possible variation with the phase angle. Indeed, the shadowing at all scales (microscopic/macroscopic) generally decreases the surface brightness of planetary surfaces with increasing phase angle. Fig. 6c corresponds to the $I/F$, normalized by

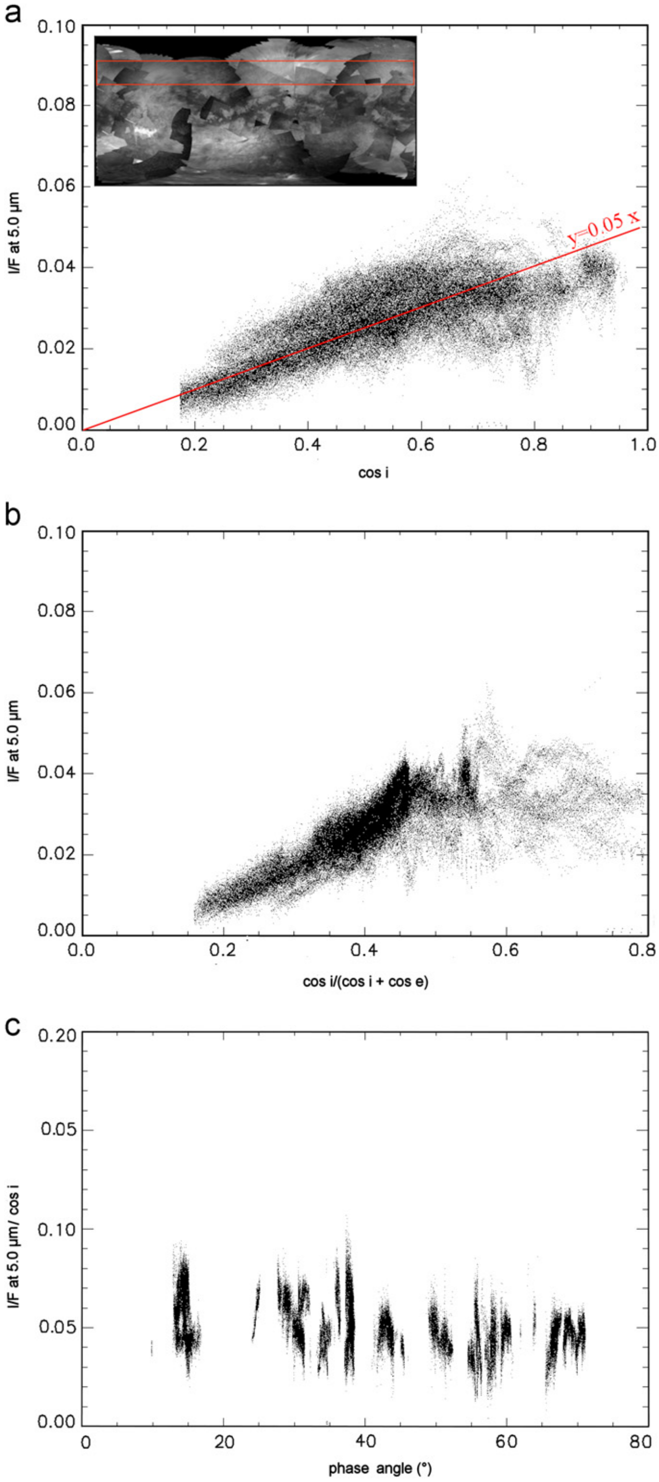

**Fig. 6.** 2D scatter plot of the I/F at 5 μm versus the cosine of the solar incidence angle in the upper panel (Lambertian case) and versus cos $i$/(cos $i$+cos $e$) in the middle panel (Lommel–Seeliger case). The plot is restricted to the points indicated by the red rectangle, which contains almost only bright terrains. The straight line in the upper panel corresponds to a pure slope of 0.05. The bottom plot corresponds to the $I/F$ divided by cos $i$ versus the phase angle in degrees. These scatter plots indicate that Titan bright terrains acts at first order as a rather Lambertian surface at 5 μm. (For interpretation of the references to color in this figure legend, the reader is referred to the web version of this article.)

Please cite this article as: Le Mouélic, S., et al., Global mapping of Titan′s surface using an empirical processing method for the atmospheric and photometric.... Planetary and Space Science (2012), http://dx.doi.org/10.1016/j.pss.2012.09.008

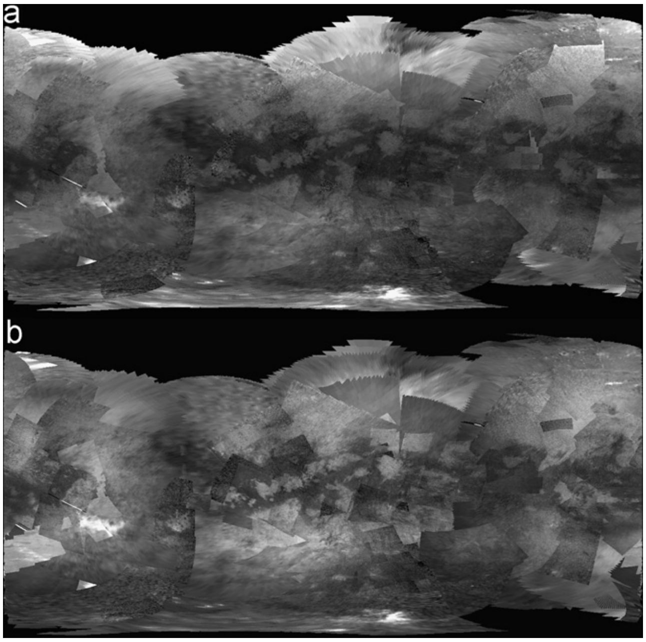

**Fig. 7.** Global mosaic at 5 μm where the viewing geometry has been normalized by dividing the $I/F$ by cos($i$) in the upper panel (Lambertian case) and cos $i$/(cos $i$ + cos $e$) in the lower panel (Lommel–Seeliger case). The mosaic is displayed with a linear grayscale between 0 (black) and 0.1 (white). These images should be compared with the uncorrected 5 μm mosaic in Fig. 4c. With only few exceptions in the northern region in the upper right corner, the normalization by the Lommel–Seeliger scattering law leaves generally more residual seams than the Lambertian case, in particular in the equatorial regions. Residual mismatch between individual frames are mostly due to transient clouds, which appear very bright at 5 μm (mostly in the polar regions and in the southern mid-latitudes), and to second order atmospheric absorptions or surface photometric effects.

cos i to correct at first order for the influence of the solar illumination, versus the phase angle. We did not observe a clear dependence between the two quantities in our area of investigation. The trends observed in Fig. 6 therefore suggest that the surface behaves at first order like a Lambertian reflector, i.e., scatters almost isotropically at 5 μm in the considered range of variations. A similar trend has been observed by Sotin et al. (2012) near Ligeia Mare. This is also consistent with the findings of Schröder and Keller (2009) at shorter wavelengths using data from the DISR instrument onboard the Huygens probe. It should be noted that the lowest value of the phase angle in our global mosaic is 4°, in a very restricted area near the equator, outside the limits of the area investigated in the plots shown in Fig. 6. There is therefore not enough data in our mosaic to accurately investigate the opposition effect, which is affecting images taken with a near zero phase angle (Schröder and Keller, 2009). The slope observed in Fig. 6a also indicates that the Titan "bright" regions have albedos at 5 μm of ~0.05 if we assume no atmospheric absorption. Our value is consistent with the work of Soderblom et al. (2009), who derived a value between 0.03 and 0.05 using a MODTRAN™ 5 radiative transfer code near Hotei Regio. Most of the light reaching the surface at 5 μm corresponds to direct flux. The important consequence of this analysis is that the division by the cosine of the incidence angle can be used to normalize at first order the viewing geometry in the 5 μm images, and therefore to correct the time and space variations of the scene illumination (Fig. 7). If we except one area mostly covered by a single cube in the upper right corner of the mosaic, we generally obtain less seams in the corrected global maps when using the cos($i$) geometric factor (upper panel of Fig.7) than when we use the Lommel–Seeliger law (lower panel of Fig. 7). This difference is particularly obvious in the equatorial regions, in the central part of the map.

The main discrepancies which are still present between individual frames in this corrected mosaic can be attributed to transient phenomena such as the very bright clouds (mainly in the polar regions and the southern mid-latitudes), and to second order atmospheric absorptions or residual surface photometric effects. We focus now on the more complex case of mosaics within the shorter wavelength atmospheric windows.

### *3.2. Correction of the short wavelength atmospheric windows: mitigating the atmospheric additive contribution*

At wavelengths shorter than 3 μm, $I_{\mathrm{scattered}}(\phi,\lambda)$ cannot be neglected anymore (Rodriguez et al., 2006). However, as was suggested in preliminary global studies by Le Mouelic et al. (2010) and in the Ontario Lacus area by Cornet et al. (2012), the wings of the atmospheric windows can be used as a proxy to empirically estimate this additive term. Indeed, for $I/F$ in a wavelength taken outside of the atmospheric window, the term $exp(-\tau_{\mathrm{atm}})$ becomes very small in eq. (1), the atmospheric additive term $I_{\mathrm{scattered}}(\phi,\lambda)$ being thus the main contributor to the observed intensity. This is also seen in the 1.22 μm image of Fig. 1 and in the global mosaic at 1.95 μm at the bottom left of Fig. 4. We use an average of the left and right band wings at characteristic wavelengths, corresponding to the first wavelengths at the shortward and longward sides respectively of a spectral window where the surface completely disappears. These wavelengths probe almost all the column of atmosphere, except the very last layers close to the ground due to the strong absorption by atmospheric gases (mainly methane). They therefore contain almost all the additive scattering contribution induced by the atmospheric haze. However, to account for the difference of gaseous absorption in the additive term in the center of the atmospheric window on the one hand, where the methane is the most transparent, and in the wings on the other hand, we empirically multiply this contribution by a scaling factor $k$. The optimum value of $k$ for a given atmospheric window at $\lambda_0$ and band wings at $\lambda_1$ and $\lambda_2$ is found by computing the least squares linear fit to the data cloud in the scatter plot of $(I/F)_{\lambda 0}-k\ \times[(\mathrm{I/F}\ )_{\lambda 1}+(\mathrm{I/F})_{\lambda 2}]/2$ versus cos($i$) for 200 values of $k$ ranging between 0.5 and 2.5, and by taking the $k$ value that minimizes the 1-sigma uncertainty estimates for the returned parameters. This computation is done exclusively on the pixels contained in the red rectangle in Fig. 6a in order to consider only surface materials of homogenous bright reflectance. This process is illustrated in Fig. 8. The left column corresponds to the 2D scatter plots without any correction. The right column shows the corresponding 2D scatter plots after substraction of the band wings with the optimized $k$-values. These corrections produce a cloud with datapoints much more linearly correlated than in the uncorrected plots, which is fully consistent with the formulation of the problem in Eq. (1). The linear fits are indicated by the plain line. The dotted lines correspond to the standard error between the data and the linear fits. Values of $k$ and parameters of the linear fits for each wavelengths of the centre of the atmospheric windows are indicated in Table 1.

We have also tested the optimization of the $k$ parameter using an alternative method, by fitting a line of the form $y=ax+b$ through the data and by finding the best $k$ value for which $b=0$. However, the images corrected by these $k$-values where visually less homogeneous and contained more residual seams than the ones found by the method based on the minimization of the points spread.

A possible physical explanation of the values of the amplification coefficients $k$ as a function of wavelength found in Table 1 can be envisaged as follows: coefficient $k$ corresponds to the amplification needed to compensate for differences in gaseous absorption between the side wavelengths and the central wavelength of a window, but in relation to the scattering effect of the

Please cite this article as: Le Mouélic, S., et al., Global mapping of Titan′s surface using an empirical processing method for the atmospheric and photometric.... Planetary and Space Science (2012), http://dx.doi.org/10.1016/j.pss.2012.09.008

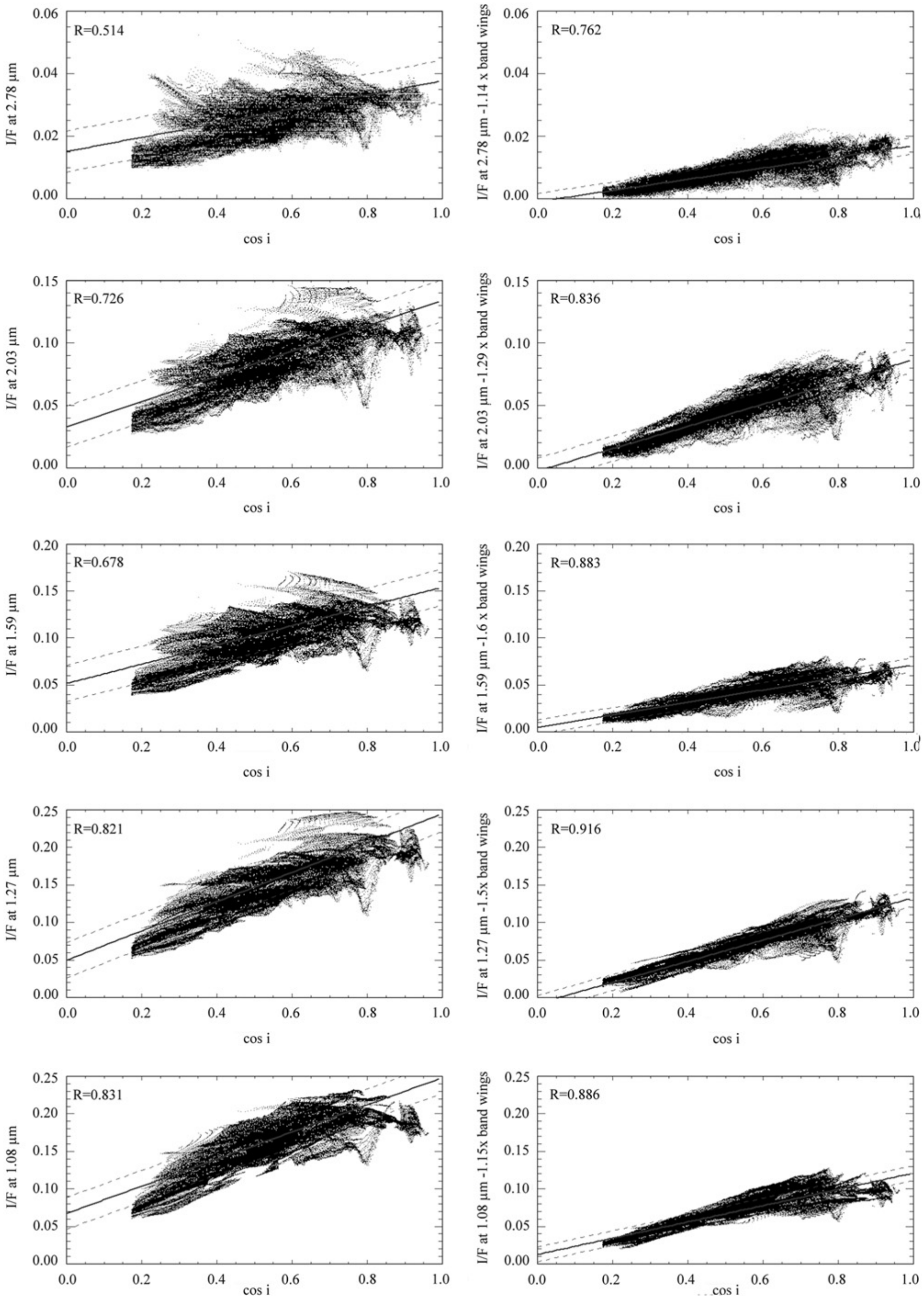

**Fig. 8.** Left, from top to bottom: plot of I/F at 2.78, 2.03, 1.59, 1.27 and 1.08 µm versus cos($i$) for the bright region contained in the red rectangle in Fig. 6a. Right: same plots after the optimized subtraction of the band wings (see details in the text). The points are much more linearly correlated after the empirical correction process. The slope of the linear fit directly relates to the mean reflectance of the bright surface at the considered wavelengths multiplied by the transmission of the atmosphere. (For interpretation of the references to color in this figure legend, the reader is referred to the web version of this article.)

**Table 1**
Parameters used for the empirical correction of the additive atmospheric term.

| Surface window wavelength (µm) | Left wing (µm) | Right wing (µm) | Coefficient k | Slope of optimized linear fit |
|---|---|---|---|---|
| 5.0 | | | | 0.05 |
| 2.78 | 2.64 | 2.83 | 1.14 | 0.018 |
| 2.03 | 1.95 | 2.13 | 1.29 | 0.089 |
| 1.59 | 1.49 | 1.65 | 1.60 | 0.066 |
| 1.27 | 1.22 | 1.32 | 1.50 | 0.141 |
| 1.08 | 1.03 | 1.14 | 1.15 | 0.108 |

aerosols. In a window at short wavelength (1.08 µm), the scattering cross section of the aerosols is high, consequently the coupling between gas and aerosols is very significant, decreasing the path length and thus the absorption, especially in the wings. Thus the needed amplification is moderate. In a window at long wavelength (2.78 µm), the scattering cross section of the aerosols is small, the coupling is weak and the path length is weakly modified. Thus the needed amplification should be important. However, at these wavelengths, the surface is dark decreasing the path length as in the first case, but for a different reason. Thus the needed amplification is also moderate. In a window at intermediate wavelength (1.59 µm), a maximum of amplification is

Please cite this article as: Le Mouélic, S., et al., Global mapping of Titan′s surface using an empirical processing method for the atmospheric and photometric.... Planetary and Space Science (2012), http://dx.doi.org/10.1016/j.pss.2012.09.008

reached resulting from the combination of a moderate coupling and an intermediate albedo.

If we assume that the additive scattering has been totally removed, the slope of the linear fit depends only on the reflectance of the soils modulated by residual photometric effects and by the absorption of atmospheric gases and aerosols.

In order to check if there is any supplementary dependence with airmass in the corrected $I/F$, we have computed the $log(I_{corr}/F/\cos(i))$ against the airmass for all surface windows, with $I_{corr}/F$ being equal to $(I/F)_{\lambda 0}-k[(I/F)_{\lambda 1}+(I/F)_{\lambda 2}]/2$, as defined previously. According to our simplified model, this quantity should be proportional to an airmass, if there is a significant extinction in the center of the windows. Fig. 9 shows the result of this analysis.

We found no obvious correlation in the test area in the bright northern region between the log of the corrected $I/F$ against the airmass, in all the atmospheric windows. This is still an important information, as it indicates either that the difference of absorption induced by the different geometric path is negligible at the considered wavelengths and geometries, or that this approach is limited by second order residual effects of the photometry on the surface signal. The objective of our paper was to correct at first order for the additive component and the geometry of acquisition. The newly performed test does not allow to go one step further into the correction process. A more detailed investigation of the effects of absorption would require a full radiative transfer model (Rannou et al., 2010), or the use of stellar and solar occultations (Bellucci et al., 2009), which falls beyond the scope of this study.

As a consequence of the previous analyses, the mosaics in the atmospheric windows can be empirically corrected for the additive atmospheric contribution by substracting the reflectance in the atmospheric window band wings multiplied by the optimized $k$ factor. Once the $I_{scattered}$ term has been mitigated in this way, a division by the cosine of the incidence angle can then be used in order to take into account, in a second step, the illumination variations, as was done for the map at 5 μm. The complete process is illustrated on final mosaics in Fig. 10 for all the atmospheric windows at wavelengths shorter than 5 μm.

We see that the applied empirical correction process provides a simple and fast tool to improve the homogeneity of the maps, and therefore represents an advantageous alternative to the use of a more complete radiative transfer modeling performed on a pixel by pixel basis, which would be too time consuming to be applied at the global scale. In addition, by using only data acquired at the time of the observation for the correction, it does not require to make assumptions on the spatial and temporal distribution of the atmospheric aerosols and gas. Fig. 11 presents an RGB color composite of the global maps corrected with our method, with the red controlled by the 5 μm image, the green controlled by the corrected 2 μm image, and the blue by the corrected 1.27 μm image. It is displayed both in cylindrical and orthographic projections. The seams have been mitigated, and differences of colors show up more clearly than in the uncorrected maps, due to the partial correction of the effect of the aerosols. These color changes translate the subtle variation in composition of Titan's surface. In particular, the dark lakes, seas and the bright potential evaporitic deposits (Barnes et al., 2011) appear very clearly in the northern hemisphere, whereas the dark brownish dunes, the bluish areas and bright terrains dominate at the equator and the tropics. We leave to further studies the detailed analysis of these regions, which falls out of the scope of this paper focused on data reduction and on the discussion of the parameters derived from the empirical approach.

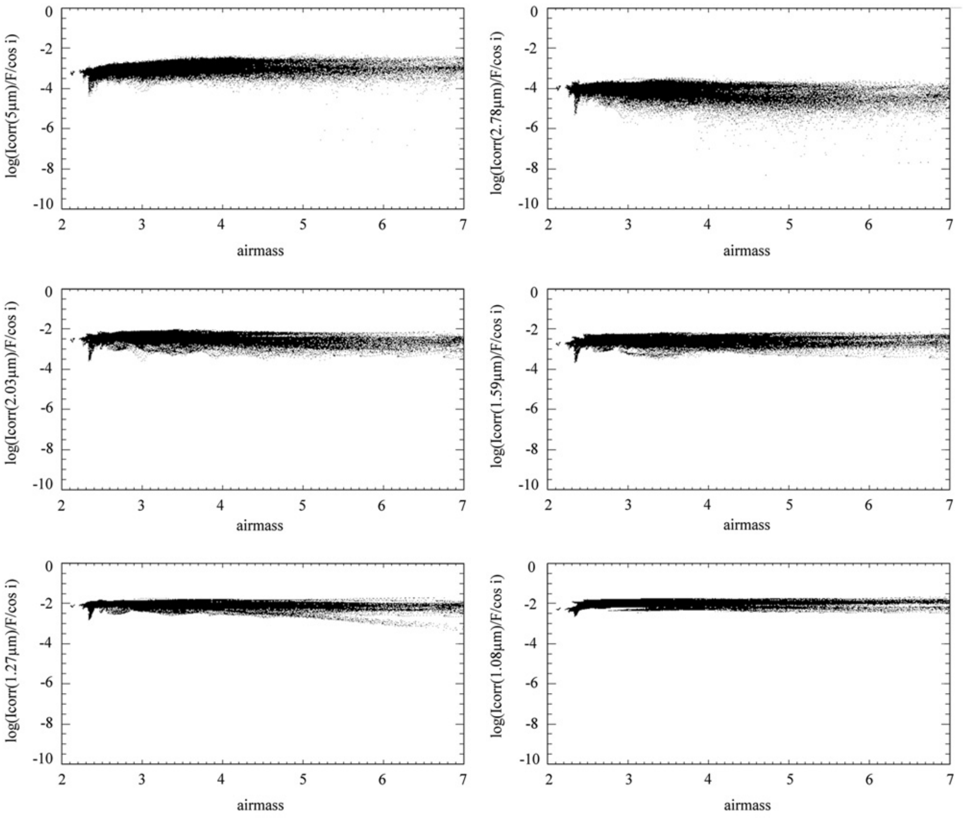

**Fig. 9.** Plots of the $\log(I_{corr}/F/\cos(i))$ against the airmass for all atmospheric windows, with $I_{corr}/F$ being equal to $(I/F)_{\lambda 0}$-$k^*[(I/F)_{\lambda 1}+(I/F)_{\lambda 2}]/2$, as defined in the text and in Table 1. The corrected $I/F$ show no significant supplementary dependence with airmass in the atmospheric windows. The plot is restricted to the points indicated by the red rectangle in Fig. 6a, which contains only bright terrains. (For interpretation of the references to color in this figure legend, the reader is referred to the web version of this article.)

Please cite this article as: Le Mouélic, S., et al., Global mapping of Titan′s surface using an empirical processing method for the atmospheric and photometric.... Planetary and Space Science (2012), http://dx.doi.org/10.1016/j.pss.2012.09.008

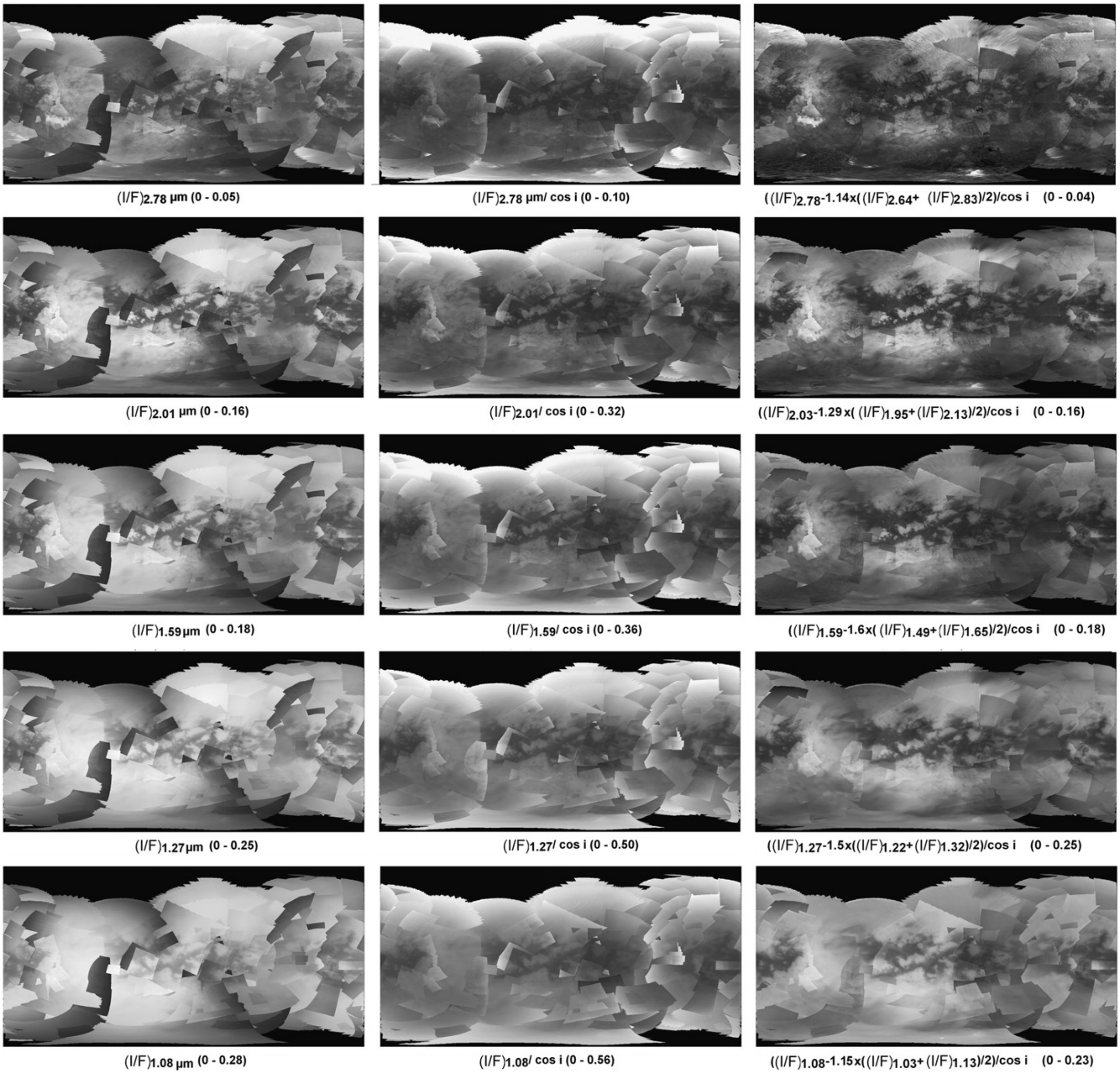

$(I/F)_{2.78\,\mu m}$ (0 - 0.05)
$(I/F)_{2.78\,\mu m}/\cos i$ (0 - 0.10)
$((I/F)_{2.78}-1.14\times((I/F)_{2.64}+(I/F)_{2.83})/2)/\cos i$ (0 - 0.04)

$(I/F)_{2.01\,\mu m}$ (0 - 0.16)
$(I/F)_{2.01}/\cos i$ (0 - 0.32)
$((I/F)_{2.03}-1.29\times((I/F)_{1.95}+(I/F)_{2.13})/2)/\cos i$ (0 - 0.16)

$(I/F)_{1.59\,\mu m}$ (0 - 0.18)
$(I/F)_{1.59}/\cos i$ (0 - 0.36)
$((I/F)_{1.59}-1.6\times((I/F)_{1.49}+(I/F)_{1.65})/2)/\cos i$ (0 - 0.18)

$(I/F)_{1.27\,\mu m}$ (0 - 0.25)
$(I/F)_{1.27}/\cos i$ (0 - 0.50)
$((I/F)_{1.27}-1.5\times((I/F)_{1.22}+(I/F)_{1.32})/2)/\cos i$ (0 - 0.25)

$(I/F)_{1.08\,\mu m}$ (0 - 0.28)
$(I/F)_{1.08}/\cos i$ (0 - 0.56)
$((I/F)_{1.08}-1.15\times((I/F)_{1.03}+(I/F)_{1.13})/2)/\cos i$ (0 - 0.23)

**Fig. 10.** From top to bottom: global cylindrical maps in the 2.78, 2.03, 1.59, 1.27 and 1.08 atmospheric windows. Left: raw $I/F$ values. Middle: $I/F$ values divided by the cosine of the incidence angle without any other correction. Right: $I/F$ values in the atmospheric windows are empirically corrected from the additive atmospheric contribution by using the subtraction of the band wings, and then divided by $\cos(i)$. The maps on the right, empirically corrected from the scattering and surface photometry, appear significantly more homogeneous than the uncorrected versions. The maps are displayed in black and white with a linear stretch corresponding to the values indicated in parenthesis.

The reddish and purplish tint towards high northern and southern latitudes are the areas observed with the least favorable geometry, and so the most difficult regions to correct for surface and atmospheric effects. We also see this effect in the Belet region, where a small subset of cubes have been acquired at very high airmass. We think that these colors are due to residual uncorrected effects of the surface photometry and atmosphere. In previous global mapping efforts by Barnes et al. (2007a) and Stefan et al. (2009), the mosaics were produced with only two flybys in the first case (T8 and T9), and with a subset of only 10 flybys in the second case, and they were not corrected from the cosine of the incidence angle. There was therefore no attempt to integrate all the VIMS images taken during all flybys (and therefore to integrate the images taken with a high spatial resolution during each closest approaches phases). Images taken during a single flyby generally provide a quite homogeneous reconstructed mosaic, due to a consistent set of observing conditions (incidence, emergence and phase) and the absence of temporal variations. Things get much more complicated when we mix up images taken during different flybys (thus with very different viewing geometries and atmospheric effects), but this is mandatory if we want to integrate the data taken with the best spatial resolution into the final mosaic.

## 4. Conclusion and perspectives

The empirical correction procedure proposed in our study represents a first step forward into the production of fully homogeneous maps of Titan's surface with the VIMS data set, paving the way for further refined algorithms. The outcomes of our empirical approach might be important to provide observational constraints

Please cite this article as: Le Mouélic, S., et al., Global mapping of Titan′s surface using an empirical processing method for the atmospheric and photometric.... Planetary and Space Science (2012), http://dx.doi.org/10.1016/j.pss.2012.09.008

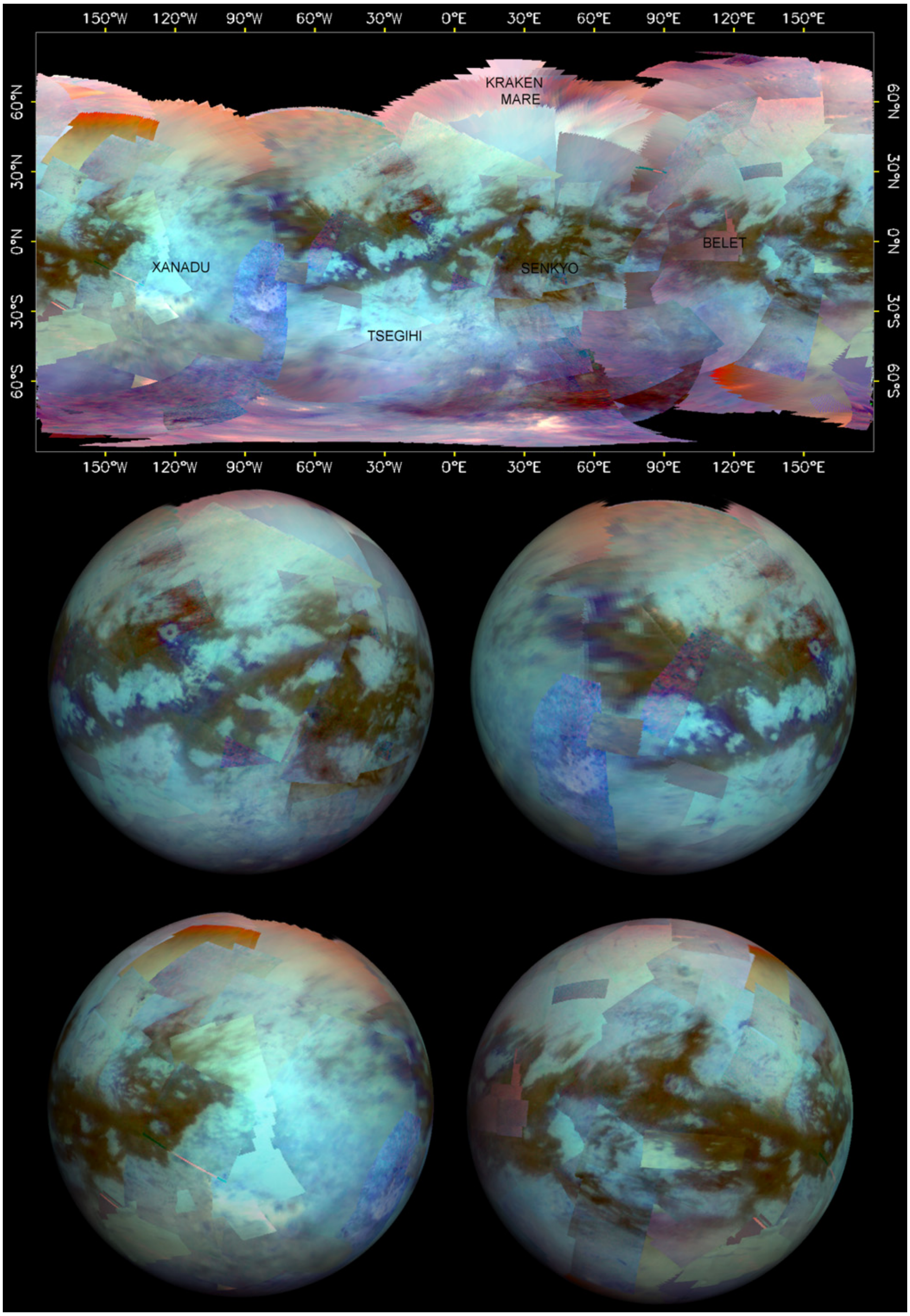

**Fig. 11.** RGB composite of the 5 μm (red), 2.03 μm (green) and 1.27 μm (blue) corrected mosaics. The upper image corresponds to a cylindrical projection. The four bottom images correspond to orthographic projections. (For interpretation of the references to color in this figure legend, the reader is referred to the web version of this article.)

and a comparison with more complete analysis performed using full radiative transfer approaches (Rannou et al., 2010). However, we also realize that there are still several sources of potential variations which should be taken into account in further studies in order to obtain fully homogenized maps. Integrating seven years of data into a synthetic map represents a challenging task, because any change in the surface (Turtle et al., 2011a, 2011b, Barnes et al., 2012) or in the atmosphere during the considered time span, which represents one season of Titan, will end up in seams. On Mars, homogeneous global maps have been acquired by the OMEGA imaging spectrometer onboard Mars Express thanks to a wealth of multidate nadir observations spanning three martian years, allowing most of the regions to be observed several times. Therefore, filtering of the data set to avoid transient atmospheric phenomena such as clouds and dust storms, seasonal surface changes such as frost cover, or effects of unfavorable viewing geometries is possible without compromising the spatial extend and resolution of the mosaic (see for example synthetic maps in Le Mouélic et al., 2009). However, because Cassini is orbiting Saturn and not Titan, the available surface coverage is much less complete than in the case of Mars. Key areas such as the northern lakes or Hotei Regio have only been observed once in acceptable viewing conditions. Hotei was observed during T48 with a spatial sampling reaching 15 km per pixel, with quite extreme geometry (e.g. Soderblom et al., 2009), producing a slightly bluish

Please cite this article as: Le Mouélic, S., et al., Global mapping of Titan′s surface using an empirical processing method for the atmospheric and photometric.... Planetary and Space Science (2012), http://dx.doi.org/10.1016/j.pss.2012.09.008

swath around 90°W. Using more restrictive constraints on the incidence, emergence, and phase angles would obviously produce mosaics with less seams, but at the expense of the global spatial coverage. This shortcoming might be overcome by the end of the Cassini mission in 2017, when more data are available.

Several improvements can be envisaged in the forthcoming studies on global mapping. First, a supplementary filter could be implemented in order to detect the pixels showing the spectral signature of clouds before including them into the final mosaic, using the semi-automated technique of Rodriguez et al. (2009, 2011). Second, the removal of the additive atmospheric component can be further improved by using a wavelength for the band wings that could be dependent of the viewing geometry, and possibly adapted image by image before being included into the final global mosaic. A specific study of the $k$ parameters on dark regions only could also be carried out. Third, a more complete surface phase function could also be derived to get rid of the residual seams of atmospherically corrected images. Photometric studies of Titan surface seem to indicate that the surface scatters rather isotropically, at least for phase angles lower than 60°, despite a strong opposition effect (Schröder and Keller, 2009, Karkoschka et al., 2011), but more complete photometric functions can still be investigated. Fourth, the radiometric calibration of the data might also be affected by variations of the solar flux during the Cassini mission, and/or stability of instrumental parameters such as the flat field, which can be further improved. Fifth, a perfect spatial registration of the data cubes would also allow the stacking (and averaging) of multidate observations, and possibly the use of a super resolution algorithm. Sixth, a correction for the a possible residual atmospheric transfer function of aerosols and gas could also be introduced. This would particularly affect the data taken at high airmass, and would therefore require the complementary use of the radiative equation with a non plane–parallel assumption. In a preliminary test, we have investigated the systematic variation of the empirically corrected $I/F$ versus the airmass in the bright northern region which served as a reference, but we found no obvious correlation in this area. This indicates that either the difference of absorption induced by the different geometric path is negligible in the corresponding atmospheric window, or that this approach is limited by second order uncorrected residual effects of the geometry on the surface signal. In the first case, this low sensitivity to the airmass might be related to the spherical nature of Titan atmosphere as regards to the radiative transfer of solar light. An alternative approach could consist in taking each VIMS observations of the same bright (or dark) reference area and to investigate their systematic variations with incidence, emergence and phase angles, assuming that there is no significant seasonal variations.

Finally, the detailed comparison between VIMS and DISR on the Huygens landing site might be useful to unlock some of the limits of the current correction methods. Indeed, the Huygens landing site has been observed by VIMS in November 2008 with a spatial sampling up to 700 m/pixel, allowing the direct comparison between VIMS spectral images and DISR mosaics and spectra taken during the descent (Sotin et al., 2009). This could provide the key to tune up both the empirical approaches and methods based on comprehensive radiative transfer models aimed at decorrelating surface and atmospheric contributions, and therefore allow VIMS to extrapolate to the global scale results derived from the local ground truth provided by Huygens.

## Acknowledgments

Authors are very grateful to two anonymous reviewers for their detailed review and very constructive comments on the original manuscript. This work benefited from financial supports from the Centre National de la Recherche Scientifique (CNRS), the Centre National d'Etudes Spatiales (CNES) and from the ANR (project APOSTIC).

## References

Barnes, J.W., Brown, R.H., Soderblom, L., Buratti, B.J., Sotin, C., Rodriguez, S., Le Mouélic, S., Baines, K.H., Clark, R., Nicholson, P., 2007a. Global-scale surface spectral variations on Titan seen from Cassini/VIMS. Icarus 186, 242–258.

Barnes, J.W., Radebaugh, J., Brown, R.H., Wall, S., Soderblom, L., Lunine, J., Burr, D., Sotin, C., S.Le, Mouélic, Rodriguez, S., Buratti, B.J., Clark, R., Baines, K.H., Jaumann, R., Nicholson, P.D., Kirk, R.L., Lopes, R., Lorenz, R.D., Mitchell, K., Wood, C.A., 2007. The Cassini RADAR Team, 2007. Near-infrared spectral mapping of Titan′s mountains and channels. Journal of Geophysical Research 112 (E11), E11006, CiteID.

Barnes, J.W., Brown, R.H., Soderblom, L., Sotin, C., le Mouélic, S., Rodriguez, S., Jaumann, R., Beyer, R.A., Buratti, B.J., Pitman, K., Baines, K.H., Clark, R., Nicholson, P., 2008. Spectroscopy, Morphometry, and Photoclinometry of Titan′s Dune fields from Cassini/VIMS. Icarus 195 (1), 400–414, http://dx.doi.org/10.1016/j.icarus.2007.12.006.

Barnes, J.W., Bow, J., Schwartz, J., Brown, R.H., Soderblom, J.M., Hayes, A.G., Vixie, G., Le Mouélic, S., Rodriguez, S., Sotin, C., Jaumann, R., Stephan, K., Soderblom, L.A., Clark, R.N., Buratti, B.J., Baines, K.H., Nicholson, P.D., 2011. Organic sedimentary deposits in Titan′s dry lakebeds: probable evaporate. Icarus 216, 136–140.

Barnes, J.W., Buratti B.J., Turtle E.P., Bow J., Dalba Pl.A., Perry J., Rodriguez S., Le Mouélic S., Baines K.H., Sotin C., Lorenz R.D., Malaska M.J., McCord T.B., Brown R.H., Clark R.N., Jaumann R., Hayne P., Nicholson P.D., Soderblom J.M., Soderblom L.A., 2012. Cassini/VIMS spectra and time-evolution of precipitation-associated surface brightening on Titan, in: Proceedings of 43rd Lunar and Planetary Science Conference, 19–23 March, The woodlands, Texas.

Bellucci, A., Sicardy, B., Drossart, P., Rannou, P., Nicholson, P.D., Hedman, M., Baines, K.H., Buratti, B., 2009. Titan solar occultation observed by Cassini/VIMS: gas absorption and constraints on aerosol composition. Icarus 201, 198–216.

Boardman, J.W., Kruse, F.A., 1994. Automated spectral analysis: a geological example using AVIRIS data, north Grapevine Mountains, Nevada: in: Proceedings of ERIM Tenth Thematic Conference on Geologic Remote Sensing, Environmental Research Institute of Michigan, Ann Arbor, MI, pp. I-407–I-418.

Brown, R.H., 2004. 21 coauthors, 2004. The Cassini Visual and Infrared Mapping Spectrometer (VIMS) investigation. Space Science Reviews 115, 111–168.

Clark, R.N., Curchin, J.M., Barnes, J.W., Jaumann, R., Soderblom, L., Cruikshank, D.P, Brown, R.H., Rodriguez, S., Lunine, J., Stephan, K., Hoefen, T.M., Le Mouélic, S., Sotin, C., Baines, K.H., Buratti, B.J., Nicholson, P.D., 2010. Detection and mapping of hydrocarbon deposits on Titan. Journal of Geophysical Research 115 , http://dx.doi.org/10.1029/2009JE003369.

Cornet, T., Bourgeois, O., Le Mouélic, S., Rodriguez, S., Lopez Gonzalez, T., Tobie, G., Fleurant, C., Sotin, C., Barnes, J.W., Brown, R.H., Baines, K.H., Buratti, B.J., Clark, R.N., Nicholson, P.D., 2012. Geomorphological significance of Ontario Lacus on Titan: integrated interpretation of Cassini VIMS, ISS and RADAR data and comparison with the Etosha Pan (Namibia). Icarus 218 (2), 788–806, http://dx.doi.org/10.1016/j.icarus.2012.01.013.

Griffith, C.A., Owen, T., Wagener, R., 1991. Titan's surface and troposphere, investigated with ground-based, near-infrared observations. Icarus 93, 362–378.

Griffith, C.A., Owen, T., Geballe, T.R., Rayner, J., Rannou, P., 2003. Evidence for the exposure of water ice on Titan's surface. Science 300, 628–630.

Hapke, B., 1993. Combined theory of reflectance and emittance spectroscopy. Cambridge University Press.

Hapke, B., Denevi, B., Sato, H., Braden, S., Robinson M., 2012. The wavelength dependence of the lunar phase curve as seen by the Lunar Reconnaissance Orbiter wide-angle camera. Journal of Geophysics. Research 117, E00H15. http://dx.doi.org/10.1029/2011JE003916.

Jaumann, R., Brown, R., Stephan, K., Barnes, J.W., Soderblom, L.A., Sotin, C., Le Mouélic, S., Clark, R.N., Soderblom, J., Buratti, B.J., Wagner, R., McCord, T., Rodriguez, S., Baines, K.H., Cruikshank, D., Nicholson, P.D., Griffith, C., Langhans, M., Lorenz, R.D., 2008. Fluvial erosion and post-erosional processes on Titan. Icarus 197, 526–538.

Jaumann, R., Kirk, R.L., Lorenz, R.D., Lopes, R.M., Stofan, E., Turtle, E.P., Keller, H.U., Wood, C.A., Sotin, C., Soderblom, L.A., Tomasko, M.G., 2009. In: Brown, R. (Ed.), Geology and surface processes on Titan (chapter 5), Titan from Cassini–Huygens. Springer Science Business Media B.V.

Karkoschka, E., Schröder, S.E., Tomasko, M.G., Keller, H.U., 2011. The reflectivity spectrum and opposition effect of Titan's surface observed by Huygens' DISR spectrometers. Planetary and Space Science 60, Issue (1), 342–355.

Le Mouélic, P., Paillou, M.A., Janssen, J.W., Barnes, S., Rodriguez, C., Sotin, R.H., Brown, K.H., Baines, B.J., Buratti, R.N., Clark, M., Crapeau, P., Encrenaz, R., Jaumann, D., Geudtner, F., Paganelli, L., Soderblom, G., Tobie, S.Wall, 2008. Mapping and interpretation of Sinlap crater on Titan using Cassini VIMS and RADAR data. Journal of Geophysical Research 113, E04003, http://dx.doi.org/10.1029/2007JE002965.

Le Mouélic, S., Combe, J-Ph, Sarago, V., Mangold, N., Massé, M., Bibring, J.P., Gondet, B., Langevin, Y., Sotin, C., 2009. An iterative least squares approach to decorrelate minerals and ices contributions in hyperspectral images: application to Cuprite (Earth) and Mars, hyperspectral image and signal processing: evolution in remote sensing. WHISPERS 26–28 (2009), 5289003, http://dx.doi.org/10.1109/WHISPERS.2009.

Please cite this article as: Le Mouélic, S., et al., Global mapping of Titan′s surface using an empirical processing method for the atmospheric and photometric.... Planetary and Space Science (2012), http://dx.doi.org/10.1016/j.pss.2012.09.008

Le Mouélic, S., Cornet, T., Rodriguez, S., Sotin, C., Barnes, J.W., Brown, R.H., Bourgeois, O., Baines, K.H., Buratti, B.J., Clark, R.N., Nicholson, P.D., 2010. Global mapping of Titan in the infrared using a heuristic approach to reduce the atmospheric scattering component, IEEE Transactions on Geoscience and Remote Sensing, Hyperspectral Image and Signal Processing: Evolution in Remote Sensing. WHISPERS 14–16.

Le Mouélic, S., Rannou, P., Rodriguez, S., Sotin, C., Griffith, C., Le Corre, L., Barnes, J.W., Brown, R.H., Baines, K.H., Buratti, B.J., Clark, R.N., Nicholson, P.D., Tobie, G., 2012. Evolution the north polar cloud on Titan monitored by The VIMS imaging spectrometer onboard Cassini. Planet. Space Science 60, 86–92, http://dx.doi.org/10.1016/j.pss.2011.04.006.

McCord, T.B., Hayne, P., Combe, J.-P., Hansen, G.B., Barnes, J.W., Rodriguez, S., Le Mouélic, S., Baines, K.H., Buratti, B.J., Sotin, C., Nicholson, P.D., Jaumann, R., Nelson, R., 2008. Cassini VIMS Team, 2008. Titan's surface: Search for spectral diversity and composition using the Cassini VIMS investigation. Icarus 194, 212–242, http://dx.doi.org/10.1016/j.icarus.2007.08.039.

Moriconi, M.L., Lunine, J.I., Adriani, A., D'Aversa, E., Negrão, A., Filacchione, G., Coradini, A., 2010. Characterization of Titan's Ontario Lacus region from Cassini/VIMS observations. Icarus 210 (2), p. 823–831.

Rannou, P., Cours, T., Le Mouelic, S., Rodriguez, S., Sotin, C., Drossart, P., Brown, R.H., Clark, R.N., Barnes, J.W., Baines, K.H., Buratti, B.J., Nicholson, P.D., 2010. Titan haze distribution and optical properties retrieved from recent observations. Icarus 208, 850–867, http://dx.doi.org/10.1016/j.icarus.2010.03.016.

Rodriguez, S., Le Mouélic, S., Sotin, C., Clénet, H., Clark, R.N., Buratti, B.J., Brown, R.H., McCord, T.B., Nicholson, P.D., Baines, K.H., 2006. and the VIMS science team, 2006. Cassini/VIMS observations of the Huygens landing site on Titan. Planetary and Space Science 54, 1510–1523.

Rodriguez, S., Le Mouélic, S., Rannou, P., Tobie, G., Baines, K.H., Barnes, J.W., Griffith, C.A., Hirtzig, M., Pitman, K.M., Sotin, C., Brown, R.H., Buratti, B.J., Clark, R.N., Nicholson, P.D., 2009. Global circulation as the main source of cloud activity on Titan. Nature 459, 78–682, http://dx.doi.org/10.1038/nature08014.

Rodriguez, S., Le Mouélic, S., Rannou, P., Sotin, C., Brown, R.H., Barnes, J.W., Griffith, C.A., Burgalat, J., Baines, K.H., Buratti, B.J., Clark, R.N., Nicholson, P.D., 2011. Titan's cloud seasonal activity from winter to spring with Cassini/VIMS. Icarus 216, 89–110, http://dx.doi.org/10.1016/j.icarus.2011.07.031.

Schröder, S.E., Keller, H.U., 2009. The unusual phase curve of Titan's surface observed by Huygens' Descent Imager/Spectral Radiometer. Planetary and Space Science 57, 1963–1974.

Soderblom, L.A., Brown, R.H., Soderblom, J.M., Barnes, J.W., Kirk, R.L., Sotin, C., Jaumann, R., Mackinnon, D.J., Mackowski, D.W., Baines, K.H., Buratti, B.J., Clairk, R.N., Nicholson, P.D., 2009. The geology of Hotei Regio, Titan: correlation of Cassini VIMS and RADAR. Icarus 204, 610–618.

Sotin, C, 2005. Release of volatiles from a possible cryovolcano from near-infrared imaging of Titan. Nature 435, 786–789.

Sotin, C., Karkoschka, E., Le Corre, L., Le Mouelic, S., Brown, R.H., Jaumann, R., Soderblom, L.A., Baines, K.H., Buratti, B.J., Clark, R.N., 2009. Comparing VIMS observations of the Huygens landing site with DISR and radar observations: implications for Titan geology and its spin rate, European Planetary Science Congress, 14–18 September, Potsdam, Germany, 316.

Sotin, C., Lawrence, K.J., Reinhardt, B., Barnes, J.W., Brown, R.H., Hayes, A.G., Le Mouélic, S., Rodriguez, S., Soderblom, J.M., Sodeerblom, L.A., Baines, K.H., Buratti, B.J., Clark, R.N., Jaumann, R., Nicholson, P.D., Stephan, K., 2012. Observations of Titan's northern lakes at 5 μm: implications for the organic cycle and geology. Icarus.

Stefan, K., Jaumann, R., Karkoschka, E., Kirk, R.L., Barnes, J.W., Tomasko, M.G., Turtle, E.P., Le Corre, L., Langhans, M., Le Mouélic, S., Lorenz, R.D., Perry, J., 2009. In: Brown, R., et al. (Eds.), Mapping Products of Titan's Surface (chapter 19), Titan from Cassini–Huygens. Springer Science Business Media B.V.

Thekekara, M.P., 1973. Solar Energy 14, 109.

Turtle, E.P., Perry, J.E., Hayes, A.G., McEwen, A.S., 2011a. Shoreline retreat at Titan's Ontario Lacus and Arrakis Planitia from Cassini imaging science subsystem observations. Icarus 212 (2), 957–959.

Turtle, EP., Perry, J.E., Hayes, A.G., Lorenz, R.D., Barnes, J.W., McEwen, A.S., West, R.A., Del Genio, A.D., Barbara, J.M., Lunine, J.I., Schaller, E.L., Ray, T.L., Lopes, R.M.C., Stofan, E.R., 2011b. Rapid and extensive surface Cchanges near Titan's equator: evidence of April showers. Science 331, 1414, http://dx.doi.org/10.1126/science.1201063.

Vixie, G., Barnes, J.W., Bow, J., Le Mouélic, S., Rodriguez, S., Brown, R.H., Cerroni, P., Tosi, F., Buratti, B.J., Sotin, C., Filacchione, G., Capaccioni, F., Coradini, A., 2012. Mapping Titan's surface features within the visible spectrum via Cassini VIMS. Planetary Space Science 60, 52–61.

Please cite this article as: Le Mouélic, S., et al., Global mapping of Titan′s surface using an empirical processing method for the atmospheric and photometric.... Planetary and Space Science (2012), http://dx.doi.org/10.1016/j.pss.2012.09.008